Characterization of structure and thermophysical properties of three ESR slags

A. Plotkowski[1], J. deBarbadillo[2], Matthew J. M. Krane[1]
[1]Purdue Center for Metal Casting Research, School of Materials Engineering
Purdue University, West Lafayette, Indiana, USA
[2]Special Metals Corporation, Huntington, West Virginia, USA

E-mail: aplotkow@purdue.edu

Abstract. The structure and properties of electroslag remelting (ESR) slags were characterized. Slags samples of three compositions were obtained from industrial remelting processes at Special Metals Corporation and from casting in a laboratory vacuum induction melter. The structure of the slag samples was observed using optical and electron microscopy, and phases were identified and their relative amounts quantified using X-ray diffraction. Laser flash thermal diffusivity, density, and differential scanning calorimetry measurements for specific heat were performed to determine the bulk thermal conductivity of the samples. Sample porosity was measured as a function of depth using a serial sectioning technique, and a one-dimensional computational model was developed to estimate the thermal conductivity of the fully dense slags. These results are discussed in context with previous studies, and opportunities for future research are identified. AFRL Case Number: 88ABW-2015-1871.

1. Introduction

The scale, cost, and complexity of the ESR process makes it difficult to investigate experimentally. Consequently, a variety of simulation efforts have been undertaken [1–4] to expand the understanding of the effects of process parameters on ingot quality. Slag property data, which are necessary inputs to such models, is sparse in the literature. Mills and coworkers [5-9] have reported solid slag results of various compositions from the ternary CaF_2-Al_2O_3-CaO and constituent binary systems. They used density, DSC, and laser flash diffusivity measurements to determine thermal conductivity. However, they produced samples via sintering and did not compare the resulting structure to actual slag skins, making it unclear if their results are relevant to ESR simulations. This study seeks to characterize the structure and thermophysical properties of solid slags taken from ESR trials, as well as some produced via solidification in a VIM. Porosity data is also reported, and a simple numerical model was developed to predict the fully dense slag conductivities.

2. Experimental Procedure

Slag samples were analyzed either in the as-received state from the ESR process, or after remelting and casting in a VIM at Purdue University. A variety of slag skin compositions were made available from ESR trials at Special Metals Corporation in Burnaugh, KY. Two compositions (Slags A and B) were chosen based on the suitability of their thickness and surface roughness for laser flash diffusivity

testing. A third composition, Slag C (Wacker Electroflux ESR2059), was investigated, but ESR samples were not available at the time of property testing, so only VIM samples (produced from virgin slag as received by Special Metals Corporation) were measured. ESR samples of Slag C later became available for microstructural characterization and measurements of phase fractions. The compositions of the three slags are shown in table 1. These values are approximate since reactions with the metal droplets are expected to alter the overall composition during the ESR process. Figure 1 shows the phase diagram of the ternary system and the approximate location of each of the slags.

Table 1. Approximate composition (in wt%) of the slags investigated.

Slag Designation	CaF_2	CaO	Al_2O_3	MgO	TiO_2
A	40	30	30	-	-
B	60	13	13	5	9
C	49.95	19.41	21.92	5.28	2.64

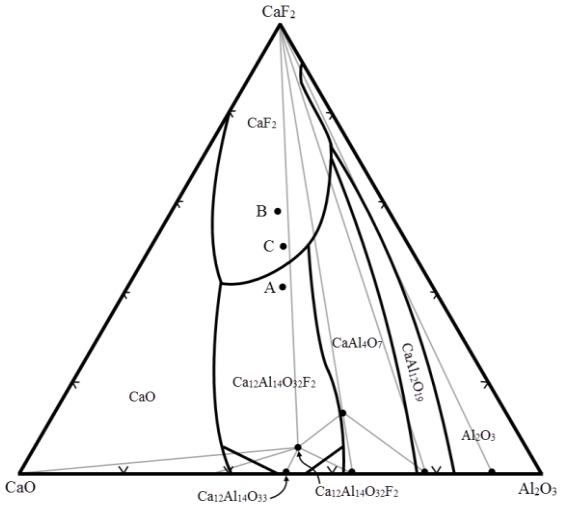

Figure 1. A simplified ternary phase diagram showing a projection of the liquidus surface and the approximate location of the three slag compositions (after Busch [10]).

VIM samples were prepared from ESR slag skins with the exception of Slag C in which VIM samples were prepared from virgin slag. VIM samples were melted in a graphite crucible in an argon atmosphere and poured into a steel mold cooled by a water cooled copper bottom plate. The microstructure of samples for the three compositions and each processing route were evaluated by optical and electron microscopy. Phases were identified via XRD and phase fractions were quantified from the XRD spectra by Rietveld refinement [11,12] using the software MAUD [13] and crystallographic data [14-17]. Busch previously found that the phases $Ca_{12}Al_{14}O_{32}F_2$ and $Ca_{12}Al_{14}O_{33}$, shown in figure 1, are practically indistinguishable via XRD, so $Ca_{12}Al_{14}O_{32}F_2$ was assumed where relevant. For electron microscopy, samples were sputter coated with Au-Pd and phase identification was performed using energy dispersive spectroscopy (EDS).

Density, specific heat, and laser flash diffusivity measurements were performed by TPRL, Inc. in West Lafayette, IN. Measurements were performed from room temperature to 1200°C. Once density, specific heat, and thermal diffusivity are measured, the thermal conductivity can be calculated:

$$k = \rho c_p \alpha \quad (1)$$

where k is thermal conductivity, ρ density, c_p constant pressure specific heat, and α thermal diffusivity.

Several samples were prepared for each condition. The slag skins tended to exhibit a layered structure, which may reduce the accuracy of the effective value determine by laser flash measurement.

However, Absi et al. [18] showed that the transient response can still give an accurate effective value of the diffusivity if the phase with the higher diffusivity accounts for less than half the volume fraction of the sample. To assess this criterion, VIM samples of slags A and C were prepared with the thin outer layer (corresponding to rapid solidification at the chill surface) removed by grinding, and their diffusivities were compared to the standard samples. Table 2 shows a summary of the samples that were prepared for thermophysical property measurements.

Table 2. Number of samples prepared for thermophysical property measurements.

Composition	ESR	VIM
A	3	2
A (1 layer)	0	2
B	3	2
C	0	5
C (1 layer)	0	2
Totals	6	13

A significant amount of porosity was observed in the ESR samples, whereas the VIM samples were comparatively sound. These samples were mounted to a steel puck using Crystalbond, and serially sectioned in the solidification direction using a surface grinder, with stereographs taken every 50 μm and pores were analyzed using ImageJ.

3. Results

Table 3 shows the phase fractions for each slag and processing route, averaged over the relevant specimens. The differences between ESR and VIM samples for Slags A and B are generally only a few weight percent. However, in Slag C, there is a significant different in $Ca_{12}Al_{14}O_{32}F_2$ content which may be attributed to the difference in composition between the ESR and VIM samples, since the VIM samples were produced from virgin slag that did not undergo reactions with metal during the ESR process.

Table 3. Summary of phase fractions (in wt.%) determined by Rietveld refinement of XRD spectra. All values are averages over several samples.

	Slag A		Slag B		Slag C	
Phase	**ESR**	**VIM**	**ESR**	**VIM**	**ESR**	**VIM**
CaF_2	31.7	27.7	44.5	44.4	49.9	48.3
$Ca_{12}Al_{14}O_{32}F_2$	68.3	72.3	0.9	1.9	40.0	44.5
$MgAl_2O_4$	-	-	20.3	18.7	-	-
$CaTiO_3$	-	-	34.3	35.0	4.1	4.3
MgO	-	-	-	-	6.0	2.9

Figure 2 shows optical micrographs comparing the structure of each slag composition between the ESR and VIM samples. Slag A shows similar phase structures between the two processing routes, beginning with a fine combination of two phases near the mold surface (bottom of the micrographs) and coarsening with distance from the mold. EDS results showed that the light phase is primary $Ca_{12}Al_{14}O_{32}F_2$ and the dark phase is CaF_2. Note the large pores in the Slag A ESR samples that are not present in the VIM micrograph.

The ESR samples of Slag B consist of three distinct layers. A fine structure near the mold surface which transitions to a middle layer containing two different precipitates in a primarily dendritic matrix with some eutectic material, and an outer layer with a courser dendritic structure containing a high fraction of interdendritic eutectic. The VIM structure is comparatively uniform containing the two precipitate phases and a complex eutectic matrix. The darker precipitates were identified as $CaTiO_3$, while the lighter are $MgAl_2O_4$. The remaining structures were found to contain all the constituent

elements, suggesting that either the volume of interaction of the electron beam for EDS was large compared to the phase size, or that one or more of the phases has a high solid solubility for the remaining elements. Similar to Slag A, the ESR samples of Slag B exhibited significant porosity (though generally less than Slag A), while the VIM samples were sound.

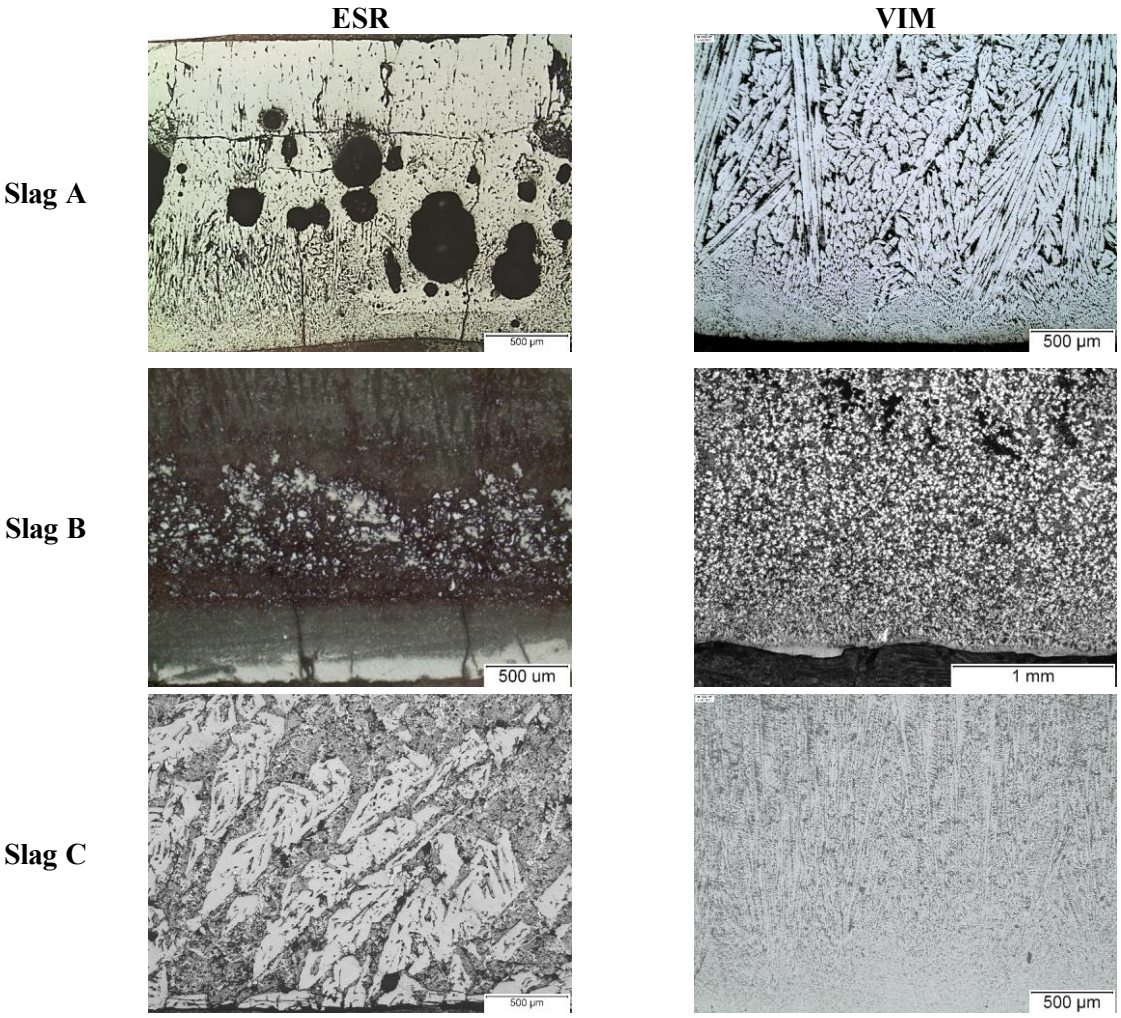

Figure 2. Optical micrographs of slag microstructures in ESR and VIM conditions. The bottom of each micrograph is nearest the chill surface.

Micrographs of the ESR and VIM processed Slag C samples show very different structures. The ESR sample shows large, faceted primary CaF_2 particles, with smaller scale complex eutectic structures composed of $Ca_{12}Al_{14}O_{32}F_2$, MgO and $CaTiO_3$. The VIM samples show multiphase dendrites, composed of CaF_2 and $Ca_{12}Al_{14}O_{32}F_2$ (based on the location in the ternary phase diagram in figure 1 and the dendrites in the ESR samples) with eutectic structures in between. These differences in structure may be attributed to changes in composition in the ESR samples relative to the virgin slag used for the VIM samples, as well as differences in cooling rate and atmosphere during solidification.

Table 4 shows a summary of the densities of the slag samples as measured by TPRL. Each data point represents the average over the relevant samples. A graphical summary of the specific heat and thermal conductivity data are given in figure 3. The single layer results are not shown, but exhibited similar or lower thermal conductivities than the bulk samples, which, according to findings by Absi et al. [18], suggests that the effective values for the multi-layered samples are accurate.

Table 4. Averaged room temperature densities for each slag composition and processing route.

Samples	Density (g/cm^3)
Slag A - ESR	2.033
Slag A - VIM	2.549
Slag A - VIM (L)	2.672
Slag B – ESR	2.544
Slag B – VIM	3.058
Slag C – VIM	2.745
Slag C - VIM (L)	2.842

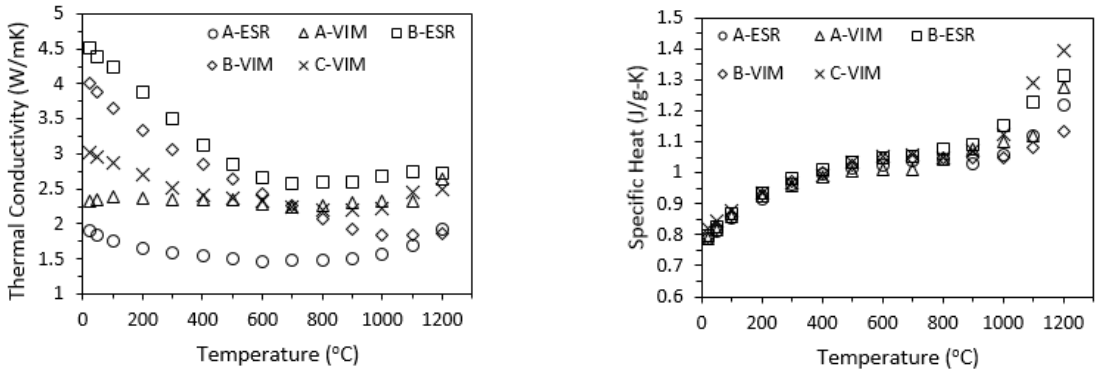

(a) *(b)*

Figure 3. (a) Thermal conductivity and (b) specific heat data obtained from TPRL, Inc. All values represent averages of data at each temperature for the multiple samples listed in table 2.

Porosity results are given in figures 4 and 5 for the ESR samples of Slags A and B, respectively, as a function of depth fraction, where zero is the metal ingot surface and one is the mold surface. In general, the pore size tends to increase with distance away from the chilled mold wall, which is consistent with experimental observations [19] of porosity in which the pore size decreases with increasing solidification rate. Additionally, the area fraction porosity tends to be small at either surface, with a maximum in the center of the sample. This result, however, may simply be a consequence of purposefully selecting slag samples with minimal surface texture for maximum suitability for the laser flash diffusivity measurements. In general, Slag A contained much larger, and more numerous pores than Slag B. Slag A also conformed to trends in pore number and size with depth better, but this may be due to increased error in identifying the small pores present in the Slag B.

4. Discussion

Comparing the thermal conductivity results for different slags and processes in figure 3 in the context of the slag microstructures reveals some interesting results. For Slag A, the VIM samples had a higher thermal conductivity than the ESR samples. The micrographs show similar phase structures, except for the significant porosity which reduces the effective conductivity of the ESR samples. However, the Slag B ESR samples showed higher conductivity than the VIM samples, despite the increased porosity in the ESR samples. This may be explained by the drastic difference in the phase structure, as seen in the micrographs in figure 2. While the phase fractions, as shown in table 3, are not very different between the two processing routes, the morphology of the phases is very different, resulting in significant changes in the thermal conductivity.

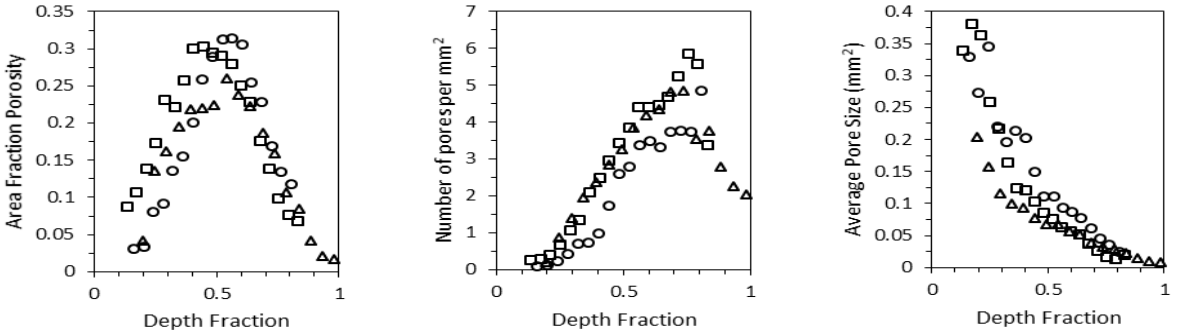

(a) *(b)* *(c)*

Figure 4. Porosity data for the three ESR samples of Slag A (○=*A-1,* □=*A-2,* and △=*A-3*). (a) Area fraction porosity, (b) number of pores per unit area, and (c) average pore area are given as a function of depth fraction, where zero is at the ingot surface and one is at the mold surface.

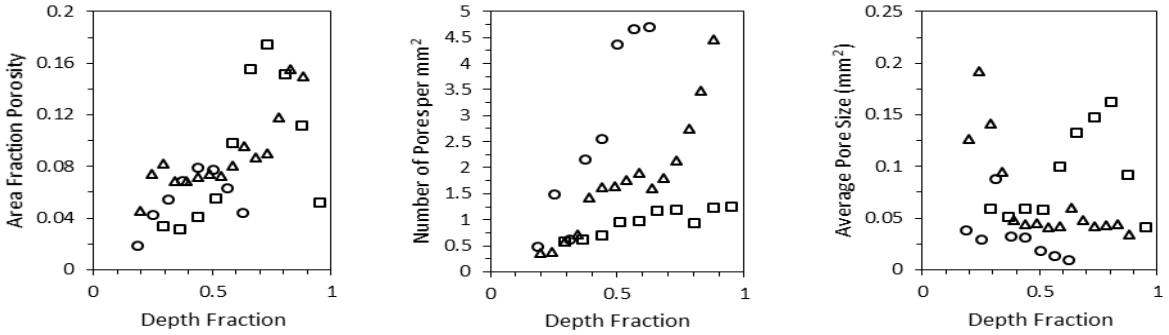

(a) *(b)* *(c)*

Figure 5. Porosity data for the three ESR samples of Slag B (○=*B-1,* □=*B-2,* and △=*B-3*). (a) Area fraction porosity, (b) number of pores per unit area, and (c) average pore area are given as a function of depth fraction, where zero is at the ingot surface and one is at the mold surface.

In an attempt to predict the fully dense slag thermal conductivity, a simple numerical model of the laser flash diffusivity test was constructed. The model is a control volume based simulation of the laser flash diffusivity test which solves the one-dimensional energy equation for heat conduction:

$$\frac{\partial T}{\partial t} = \alpha \frac{\partial^2 T}{\partial x^2}, \qquad (2)$$

where T is temperature, t is time, x is axial position, and α is the thermal diffusivity. The model first assumes a thermal conductivity for the fully dense slag. The porosity distribution data is then used to estimate the density, specific heat, and thermal conductivity of each control volume. The simulation calculates the effective thermal diffusivity based on the ASTM E1461-13 standard using equation 3. That result is compared to the actual TPRL data, and the slag conductivity is adjusted up or down appropriately and the simulation run again. This iteration continues until the simulation diffusivity is within some tolerance of the measured diffusivity:

$$\alpha = 0.13879L^2/t_{1/2}, \qquad (3)$$

where L is the sample thickness and $t_{1/2}$ the time required for the backside of the sample to reach half of its maximum temperature.

The porosity contributes only negligibly to the mass and specific heat so that these properties may be estimated using the volume fraction porosity directly. The effective thermal conductivity was estimated using a variety of models taken from the literature. The first is the series model or arithmetic mean shown in equation 4. This gives the maximum possible effective thermal conductivity value and

minimum slag conductivity [20,21]. The corresponding minimum effective value is a parallel model, or harmonic mean which was found to give unrealistically high slag conductivity predictions. An intermediate between the parallel and series models is the geometric mean [20] as shown in equation 5.

Maxwell's model for randomly dispersed, non-interacting spheres, derived for electrical conductivity, is shown in equation 6 [22], and has shown good agreement with experiments for effective thermal conductivities [23]. Bruggeman's model [24] in equation 7 was derived in a similar manner to Maxwell's model, but with different assumptions about the permeability and electric field strength, and has been found to be more accurate than Maxwell's model at predicting effective thermal conductivities at high volume fractions of the dispersed phase [25,26]. Russell [27] proposed a model (equation 8) based on cubic pores using the laws for parallel and series resistances, which has been found to be accurate within 10% for porous materials [28]. All of the models are summarized in table 5, where k_m is the effective sample conductivity, k_s the slag conductivity, k_p the pore conductivity, and φ the volume fraction porosity.

The results of the numerical model are shown in figure 6. It is clear that the geometric relationship over predicts the slag conductivity, while the remaining four models produce similar results. From figure 6a, it appears that porosity alone cannot explain the differences between the ESR and VIM samples for Slag A. It may be concluded that there is some contribution from differences in phase structure or experimental error. Predictions for Slag B in figure 6b reinforce the effect of the phase structure on the effective properties, since the effect of correcting the ESR thermal conductivity values for porosity produces higher values than the fully dense VIM samples.

Table 5. Summary of effective thermal conductivity models.

Series Model:	$k_m = (1-\phi)k_s + \phi k_p$	*(4)*
Geometric Mean:	$k_m = k_s^{(1-\phi)} k_p^{\phi}$	*(5)*
Maxwell:	$k_m = \frac{k_s\left[k_p + 2k_s - 2\phi\left(k_s - k_p\right)\right]}{k_p + 2k_s + \phi\left(k_s - k_p\right)}$	*(6)*
Bruggeman:	$\frac{k_m - k_p}{k_s - k_p}\left(\frac{k_s}{k_m}\right)^{1/3} = 1 - \phi$	*(7)*
Russell:	$k_m = k_s \frac{\phi^{2/3} + \frac{k_s}{k_p}\left(1 - \phi^{2/3}\right)}{\phi^{2/3} - \phi + \frac{k_s}{k_p}(1 - \phi^{2/3} + \phi)}$	*(8)*

5. Conclusions

The microstructures, phase fractions, and thermophysical properties of three ESR slag compositions were characterized for two different processing routes. It was found that the phase content, phase fractions, porosity content, and phase morphology all contributed to the effective thermophysical properties. A numerical model of the laser flash diffusivity test was designed to predict the fully dense slag thermal conductivity as a function of porosity. These results reinforced the conclusion that the combination of phase structure and porosity content affect the thermophysical properties of slag skins.

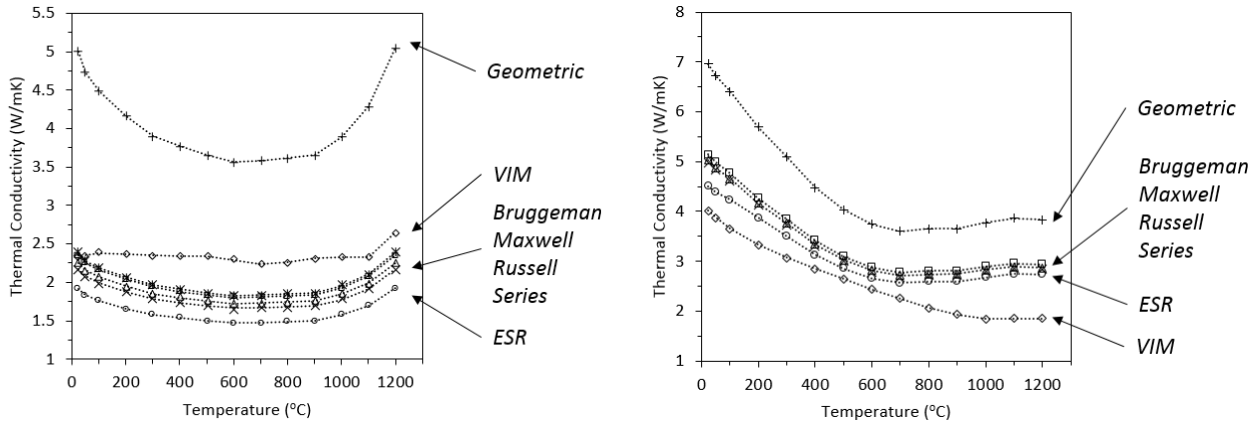

Figure 6. Predicted fully dense slag thermal conductivities for (a) Slag A and (b) Slag B.

6. References

[1] Kharicha A, Mackenbrock A, Ludwig A, Schützenhöfer W and Maronnier V 2007 *Int. Symp. Liq. Met. Process. Cast.* 113-20
[2] Weber V, Jardy A, Dussoubs B, Ablitzer D, Rybéron S, Schmitt V, Hans S and Poisson H 2009 *Metall. Mater. Trans. B* **40** 271-80
[3] Kelkar K M *et al.* 2013 *Proc. 2013 Int. Symp. Liq. Met. Process. Cast.* 3–12.
[4] Yanke J, Fezi K, Trice R and Krane M J M 2014 *Numer. Heat Transf. Part A Appl.* **67** 268–92
[5] Mills K C, Powell J S, Bryant J W and Keene B J 0981 *Can. Metall. Q.* **20**, 93–9
[6] Keene B J and Mills K C 1981 *Arch. Fur Das Eis.* **52** 311–15
[7] Gohil D D and Mills K C 1981 *Arch. Fur Das Eis.* **52** 335–40
[8] Morrell R and Mills K C 1981 *Arch. Fur Das Eis.* **52** 381–3
[9] Taylor R and Mills K C 1982 *Arch. Fur Das Eis.* **53** 55–63
[10] Busch J D 2012 M.S. thesis, Purdue University
[11] Rietveld H M 1967 *Acta Crystallogr.* **22** 151–2
[12] Bish D L and Howard S A 1988 *J. Appl. Crystallogr.* **21** 86–91
[13] Lutterotti L, Matthies S and Wenk H R 1999 *IUCr Newsl. CPD* **21** 14–5
[14] Gražulis S *et al.* 2009 *J. Appl. Crystallogr.* **42** 726–9
[15] Gražulis S *et al.* 2012 *Nucleic Acids Res.* **40** 420–7
[16] Bergerhoff G and Brown I D 1987 *Int. Union Crystallogr. Chester* 77–95
[17] Belsky A, Hellenbrandt M, Karen V L and Luksch P 2002 *Acta Crystallogr. Sect. B* **58** 364–9
[18] Absi J, Smith D, Naït-Ali B, Grandjean S and Berjonnaux J 2005 *J. Eur. Cer. Soc.* **25** 367–73
[19] Lee P, Hunt J 1997 *Scr. Mat.* **36** 399-404
[20] Woodside W and Messmer J H 1961 *J. Appl. Phys.* **32** 1688–99
[21] Progelhof R C, Throne J L and Ruetsch R R 1976 *Polym. Eng. Sci.* **16** 615–25
[22] Maxwell J C 1904 *A Treatise on Electricity and Magnetism* (Oxford: Clarendon Press)
[23] Sakiyama T, Matsushita Y, Shiinoki Y, and Yano T 1990 *J. Food Eng.* **11** 317–31
[24] Bruggeman V 1935 *Ann. Der Phys.* **5** 636–64
[25] Wang B, Zhou L and Peng X 2003 *Int. J. Heat Mass Transf.* **46** 2665–72
[26] Lee T Y R and Taylor R E 1978 *J. Heat Transfer* **100** 720–4
[27] Russell H W 1935 *J. Am. Ceram. Soc.* **18** 1–5
[28] Cheng S C and Vachon R I 1970 *Int. J. Heat Mass Transf.* **13** 537–46

Acknowledgements
The authors would like to acknowledge the support of the Metals Affordability Initiative, AFRL Case Number: 88ABW-2015-1871, and Special Metals Corporation for supplying samples.